

Provided for non-commercial research and education use.  
Not for reproduction, distribution or commercial use.



This article appeared in a journal published by Elsevier. The attached copy is furnished to the author for internal non-commercial research and education use, including for instruction at the authors institution and sharing with colleagues.

Other uses, including reproduction and distribution, or selling or licensing copies, or posting to personal, institutional or third party websites are prohibited.

In most cases authors are permitted to post their version of the article (e.g. in Word or Tex form) to their personal website or institutional repository. Authors requiring further information regarding Elsevier's archiving and manuscript policies are encouraged to visit:

<http://www.elsevier.com/copyright>



Contents lists available at ScienceDirect

## Journal of Non-Newtonian Fluid Mechanics

journal homepage: [www.elsevier.com/locate/jnnfm](http://www.elsevier.com/locate/jnnfm)

## Extensional dynamics of viscoplastic filaments: II. Drips and bridges

Neil J. Balmforth, Neville Dubash, Anja C. Slim\*

Department of Mathematics, 1984 Mathematics Road, University of British Columbia, Vancouver, BC V6T 1Z2, Canada

## ARTICLE INFO

## Article history:

Received 10 August 2009

Received in revised form 8 May 2010

Accepted 29 May 2010

## Keywords:

Viscoplastic fluids

Surface tension

Pinch-off

## ABSTRACT

A model for the dynamics of slender filaments of Herschel–Bulkley fluid is used to explore viscoplastic dripping under gravity and thinning under controlled extension (liquid bridges). The conditions required for fluid to yield are delineated, and the subsequent thinning and progression to pinch-off are tracked numerically. Calculations varying the dimensionless parameters of the problem are presented to illustrate the effect of surface tension, rheology, inertia (for dripping) and gravity. The theoretical solutions are compared with laboratory experiments using aqueous solutions of Carbopol and Kaolin suspensions. For drips and bridges, experiments with Carbopol are well matched by the theory, using a surface tension equal to that of water, even in situations when the fluid is not slender. Experiments with Kaolin do not compare well with theory for physically plausible values of the surface tension. Implications for rheometry and surface-tension inference are discussed.

© 2010 Elsevier B.V. All rights reserved.

## 1. Introduction

In the first of this duet of papers on the dynamics of viscoplastic filaments, we derived a slender-thread model and applied it to the classical Rayleigh instability problem. For Newtonian fluids, the Rayleigh instability provides the simplest theoretical setting in which to study the competition between surface tension and viscous stress with or without inertia [1]. As discussed in the prequel, the viscoplastic version of the Rayleigh instability should not be so regarded: a uniform filament is rigidly held by the yield stress and cannot be deformed by a linear perturbation; the Rayleigh instability is therefore completely removed, and a finite-amplitude initial disturbance is required to initiate any thinning of the filament. Unfortunately, the dependence of the resulting dynamics on the form of the initial perturbation renders the problem more artificial and unphysical.

By contrast, the two problems we now move on to consider, viscoplastic dripping and extending bridges (illustrated in Fig. 1), are more natural since fluid flow does not need to be initiated by introducing a predefined deformation to an existing cylindrical filament. Moreover, the two problems are simpler to set up and study in the laboratory. Indeed, extending bridges are the central flow device used in some rheometers to infer extensional viscosity. Both problems have been extensively investigated for Newtonian and viscoelastic fluids; comprehensive reviews and pertinent references are provided by Eggers [1] and Eggers and Villermaux [2].

The ease of setting up analogous laboratory studies enables us to complement our theoretical discussion of drips and bridges with experiments that provide a firmer connection with the practicalities of rheometry as well as a test of the theoretical predictions. As proto-typical viscoplastic fluids, we use Carbopol solutions and Kaolin slurries, which are commonly assumed to possess both a yield stress and a shear-thinning viscosity. However, neither fluid is ideal, with a number of previous studies providing evidence for flow behaviour that cannot be captured by a simple Herschel–Bulkley rheology [3–5]. In fact, a secondary objective in the current work is to further quantify such non-ideal behaviour by detecting disagreements between the theory and experiments. As we shall see, the extensional dynamics of Carbopol filaments appear to be well modelled by the theory, but Kaolin filaments are more problematic.

The dripping of viscoplastic fluids has recently been addressed in a number of studies: a numerical simulation for the pinch-off of a drop of Bingham fluid was presented by Davidson and Cooper-White [6]; although this simulation avoids any assumption of slenderness, only limited results are reported presumably because of the increased computational complexity. Al Khatib and Wilson [7] and Coussot and Gaulard [8] modelled slender drops of inertialess viscoplastic filaments without surface tension and presented solutions for a single set of parameters. In this situation, a drop falls from the end of the extruded filament once the gravitational pull surpasses the yield stress, but the drop remains connected by an infinitely drawn-out thread. Surface tension and inertia are essential to obtain pinch-off at a finite length. Coussot and Gaulard compared the drop volumes predicted by this theory with experiments using a number of different viscoplastic materials, finding reasonable quantitative agreement for a commercial

\* Corresponding author.

E-mail address: [aslim@fas.harvard.edu](mailto:aslim@fas.harvard.edu) (A.C. Slim).

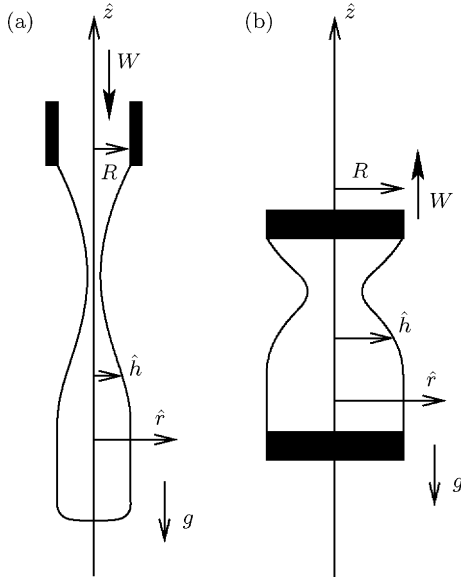


Fig. 1. The geometry of the (a) dripping and (b) bridge problems. The profiles shown are numerical solutions of the reduced model equations.

hair gel and a certain degree of qualitative agreement for other viscoplastic fluids. The current article extends these works by adding surface tension and inertia, examining parameter space and by making more demanding comparisons between the slender theory and experiments. The only work that we are aware of directed at viscoplastic bridges is an unpublished manuscript by A. Alexandrou (personal communication) that presents numerical computations using a different extension protocol (i.e., motion of the adjoining plates) to the one adopted here (we consider a fixed rate of extension; Alexandrou's plates are brought to rest after an initial transient). Some attention has been directed at the limit of very squat bridges, corresponding to the problem of adhesion. In this case, the flow is no longer primarily extensional and our description does not apply. However recently Barral et al. [9] applied a simplified, plastic lubrication model to the problem and obtained some agreement with experiments.

Although there are a large number of applications of our analysis in engineering, the dynamics of viscoplastic filaments also has a great deal of interest due to the basic physics and the implications for rheometry. Notably, the pinch-off problem traverses the full physical range of deformation rate (in this case, the rate of extension), beginning from the yielding of a rigid column to the nearly singular extension rates arising near pinch-off. Thus, one wonders whether this "sampling" of the full behavioural range can be harnessed to provide a relatively complete picture of fluid rheology. Equally as importantly, however, many standard prescriptions for determining surface tension are obscured by the presence of a yield stress (as surface tension is not able to deform the fluid surface if the curvatures and applied stresses are too small), leaving one needing alternative methods for the task. In order to address these questions, we offer several reflections on the implications of the theoretical results for rheometry and surface-tension inference.

## 2. Theoretical model

The dimensionless equations of motion determining the radius,  $h(z, t)$ , and axial speed,  $w(z, t)$ , of a slender viscoplastic filament are (see paper I)

$$\frac{\partial h}{\partial t} + w \frac{\partial h}{\partial z} = -\frac{1}{2} h \frac{\partial w}{\partial z}, \quad (1)$$

$$\mathcal{R} \left( \frac{\partial w}{\partial t} + w \frac{\partial w}{\partial z} \right) = -\frac{\partial \kappa}{\partial z} + \frac{3}{2h^2} \frac{\partial}{\partial z} (h^2 \tau_{zz}) - G, \quad (2)$$

where the curvature is

$$\kappa = \frac{1}{h [1 + (\partial h / \partial z)^2]^{1/2}} - \frac{\partial^2 h / \partial z^2}{[1 + (\partial h / \partial z)^2]^{3/2}}, \quad (3)$$

and the Herschel–Bulkley constitutive relation is written as

$$\frac{\partial w}{\partial z} = \frac{1}{\sqrt{3}} \text{sgn}(\tau_{zz}) \left[ \max \left( \frac{\sqrt{3}}{2} |\tau_{zz}| - \beta, 0 \right) \right]^{1/n} \quad (4)$$

(accommodating the yield condition,  $|\tau_{zz}| > 2\beta/\sqrt{3}$ ). In arriving at this dimensionless system, axial lengths and radii have been scaled by  $R$ , the radius of the thread where it is either extruded from a pipe (for the dripping problem) or attached to adjoining plates (for the bridges; see Fig. 1), times are scaled with the viscous–capillary time-scale,  $T = (KR/\gamma)^{1/n}$  (where  $K$  is the consistency of the Herschel–Bulkley relation, and  $\gamma$  is the surface tension), speeds with  $R/T$ , and stresses and pressure with  $KT^{-n}$  (with  $n$  the Herschel–Bulkley power-law index). The dimensionless parameters are

$$\mathcal{R} = \frac{\rho R^3}{\gamma} \left( \frac{\gamma}{KR} \right)^{2/n}, \quad G = \frac{\rho g R^2}{\gamma}, \quad \beta = \frac{\tau_Y R}{\gamma}.$$

For the current problems, we also have the dimensionless extrusion or extension speed,

$$\mathcal{W} = \frac{W}{R} \left( \frac{KR}{\gamma} \right)^{1/n},$$

which can be interpreted as the ratio of the time-scale for extrusion or extension to the time-scale of the viscous–capillary reaction, or a modified capillary number.

We solve Eqs. (1)–(4) numerically using the scheme described in Appendix A. The initial configuration and boundary conditions are specific to each of the problems that we study and are summarized at the beginning of Sections 3 and 4.

## 3. Dripping

To explore gravitationally induced dripping, viscoplastic fluid is extruded at a fixed speed through a vertical, cylindrical pipe (Fig. 1a). The boundary conditions at the pipe's orifice are  $h(0, t) = 1$  and  $w(0, t) = -\mathcal{W}$ . The base of the pendant drop,  $z = L(t)$  with  $dL/dt = w(L, t)$ , is a free boundary that must be computed as part of the problem.

A second boundary condition is required at the base of the drop. Partly for numerical reasons, we consider two different cases: first, the most natural choice is  $h(L, t) = 0$ . Unfortunately, this choice complicates the initial condition because  $h(z, 0)$  must be continuous for our numerical scheme to compute the solution reliably. To begin, we therefore follow previous researchers (e.g., [10]) and introduce a rigidly moving spherical cap that protrudes to  $L(0) = -0.1$ , so that  $h(z, 0) = \sqrt{1 - z^2/L(0)^2}$  and  $w(z, 0) = -\mathcal{W}$ . However, a further complication with this initial condition is that because of the shape of the spherical cap surface tension can drive flow adjustments near the tip that do not affect the dynamics higher up the filament but which require proper but superfluous resolution throughout the computation (see Section 3.1). This motivates the second choice for the lower boundary condition.

Provided curvatures are dominated by the leading-order term,  $\kappa \approx 1/h$ , the conservative form of (2) is

$$\mathcal{R} \left[ \frac{\partial}{\partial t} (h^2 w) + \frac{\partial}{\partial z} (h^2 w^2) \right] = \frac{\partial}{\partial z} \left( h + \frac{3}{2} h^2 \tau_{zz} \right) - Gh^2. \quad (5)$$

Thus, if

$$\tau_{zz}(L, t) = -2/3, \quad h(L, t) = 1, \quad (6)$$

then the end of the thread freely falls under gravity, maintaining its thickness and remaining unyielded if  $\beta > 1/\sqrt{3}$ . In other words, the “free-tip” conditions (6) introduce no dynamics near the tip, leading to a solution that furnishes the correct gravitational stress on the higher regions of the filament where thinning occurs. Thus, this second choice allows us to begin with  $h(z, 0) = 1$  (and  $L(0) = -0.1$ ) and compute solutions without needing to resolve any tip dynamics (at least provided the yield stress is not too small,  $\beta > 1/\sqrt{3}$ ), expediting the computation.

We continue both sets of computations well beyond the moment that the upper regions of the thread begin to yield under the weight of the underlying material and up to the moment that the filament thins to a minimum radius of  $h_{\min} = 0.05$ . We end the computations before the final pinch-off for the technical reasons that are given presently and because we are chiefly interested in the larger scale features of drop formation rather than the pinch-off dynamics which (as elucidated in part I) is dominated by the viscous stresses (Newtonian or power-law) and is therefore captured by existing theory. In comparisons with experiments we compute profiles further, to  $h_{\min} = 10^{-3}$ .

### 3.1. Inertialess drips ( $\mathcal{R} = 0, \mathcal{W}$ finite)

We begin with a discussion of the inertialess problem, which allows some analytical inroads and a faster exploration of parameter space. A sample numerical solution using the boundary condition  $h(L, t) = 0$  is shown in Fig. 2. Although fresh material is extruded from the orifice in an unyielded state, the high curvature associated with the initial spherical cap generates a stress that liquefies the tip of the extrusion (as mentioned above). The rela-

tively small yielded tip persists throughout the computation and is attached to an overlying plug that is rigidly pushed out until the weight of the filament is sufficient to liquefy the thread a second time near the orifice. Thinning in this upper yielded region is qualitatively similar to the inertialess Newtonian case, with an almost up-down symmetric neck and the minimum radius occurring near the centre of the region.

Although the detailed adjustment in the vicinity of the tip is dependent on the particular choice of initial condition, the dynamics further up the thread is insensitive to this choice. This is illustrated in panel (e) of Fig. 2 which compares the thread profile at the end of the computation shown in the rest of that figure with an equivalent profile from a computation using the alternative boundary condition in (6). The unyielded, squared end of the second computation is clearly revealed in the picture, yet differences in the upper portions of the thread, including the upper yield surface, can barely be distinguished. Thus, we conclude that the tip dynamics does not affect the manner in which the thread thins further up. In particular, we anticipate the same behaviour even if we were to begin the evolution from a previous pinch-off event (as in the experiments).

In the absence of surface tension and inertia, the limiting length of a viscous thread is infinite when pinch-off eventually occurs [11]. We also find this result here, even when including surface tension and viscoplasticity, and below we offer a mathematical explanation (Wilson [11] also recognized that surface tension does not modify the eventual pinch-off, but gives no detailed reasoning). An awkward consequence of the infinite extension of the inertialess thread is that we are unable to continue computations until the final moment of pinch-off, motivating the halt of the computation when the minimum radius  $h_{\min} = 0.05$ . An alternative is to reintroduce inertia, which causes pinch-off at finite length when there is no yield stress (at least with moderate values of  $n$  [12]), and likely remains true here because viscous stresses dominate the yield stress at pinch-off. Nevertheless, our main thrust is to explore the effect of a yield stress, and so we simply stop the computations at finite, but relatively small radius.

#### 3.1.1. Drop volume

An analytical prediction can be made for the volume of the pinched-off drop if we introduce the asymptotic approximation,  $\kappa \approx 1/h$ , together with a Lagrangian coordinate system,  $(z_0, t)$ , where  $z_0 = \mathcal{W}t_0$  and  $t_0$  is the time that a fluid slice leaves the orifice, or  $z_0$  is the initial location of a fluid slice within the supply pipe (cf., [11]). Conservation of mass implies  $\partial z/\partial z_0 = 1/h^2$  and the vertical momentum Eq. (2) integrates to

$$\frac{3}{2}h^2\tau_{zz} = Gz_0 - h,$$

on imposing the free-tip condition (6).

Eq. (1) now becomes

$$\begin{cases} h = 1, & z_0 \leq z_{0Y} \\ \frac{\partial h}{\partial t} + \frac{1}{2\sqrt{3}}h\left(\frac{Gz_0 - h}{\sqrt{3}h^2} - \beta\right)^{1/n} = 0, & z_0 > z_{0Y}, \end{cases} \quad (7)$$

where

$$z_{0Y} = (\sqrt{3}\beta + 1)/G$$

is the initial location of the first fluid slice to yield in tension. Thus,

$$t - \frac{z_0}{\mathcal{W}} = \int_1^{1/h} \frac{2\sqrt{3}}{y(Gz_0y^2/\sqrt{3} - y/\sqrt{3} - \beta)^{1/n}} dy. \quad (8)$$

To determine the drop volume, we set  $h = 0$  in (8) to give the time  $t_c(z_0)$  at which a slice initially at  $z_0$  achieves zero radius. Searching for the minimum of this function,  $\partial t_c/\partial z_0 = 0$ , then provides the

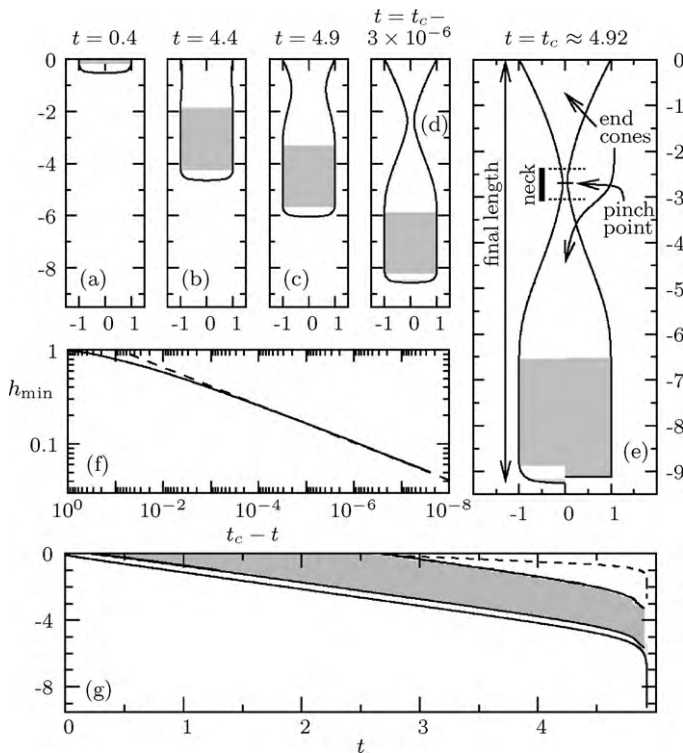


**Fig. 2.** Inertialess drop for  $\mathcal{W} = G = \beta = 1$  and  $n = 0.4$ . (a–e) Profiles at different times; shaded regions are unyielded. In (e), the right-hand-side shows the free-tip solution. (f) Log–log plot of minimum thread radius against  $t_c - t$ ; dashed curve is (11). (g) Position of base of drop, unyielded region (shaded) and minimum radius location (dashed) against time. ( $N = 200$  grid points.)

initial location of the pinch-point,  $z_0 = z_{0P}$ . After some algebra we arrive at the implicit expression,

$$\frac{z_{0P}}{\mathcal{W}} = \sqrt{3} \left( \frac{\sqrt{3}}{G(z_{0P} - z_{0Y})} \right)^{1/n} + \left( \frac{\sqrt{3}}{Gz_{0P}} \right)^{1+1/n} \times \frac{{}_2F_1(1 + 2/n, 1 + 1/n; 2 + 2/n; 2M/(m + M))}{(2 + n)(m + M)^{1+2/n}}, \quad (9)$$

where  $m = 1 - 1/2Gz_{0P}$ ,  $M = \sqrt{z_{0Y}/z_{0P} - 1 + m^2}$  and  ${}_2F_1(\cdot, \cdot; \cdot; \cdot)$  is the hypergeometric function [13]. The drop volume is then  $\pi z_{0P}$ . Predictions from (9) are accurate provided inertia and the omitted curvature term are negligible. Simpler expressions follow in the limit of small extrusion speed where growth is quasi-static; surface tension then allows pinch-off to occur rapidly once the yield stress is overcome. In this circumstance,  $z_{0P} \sim z_{0Y}$ , giving the simplest estimate for the drop volume of  $(\sqrt{3}\beta + 1)\pi/G$ . Substituting  $z_{0P} = z_{0Y}$  into the left-hand side of (9) provides the improvement,

$$z_{0P} \approx z_{0Y} + \frac{\sqrt{3}}{G} \left( \frac{\sqrt{3}\mathcal{W}}{z_{0Y}} \right)^n. \quad (10)$$

3.1.2. Minimum radius near pinch-off

The Lagrangian framework can also be used to predict the asymptotic approach to pinch-off: for small  $h$ , the yield stress and surface tension terms can be neglected from (7) to furnish

$$\frac{\partial h}{\partial t} \sim -\frac{1}{2\sqrt{3}} \left( \frac{Gz_0}{\sqrt{3}} \right)^{1/n} h^{1-2/n}.$$

We find a limiting solution as  $t \rightarrow t_c$ ,

$$h_{\min} \sim \left( \frac{1}{n\sqrt{3}} \right)^{n/2} \left( \frac{Gz_{0P}}{\sqrt{3}} \right)^{1/2} (t_c - t)^{n/2}, \quad (11)$$

which is compared to the numerical results in Fig. 2f. This solution reflects how the dominant balance is between viscous stresses and gravitational forcing near pinch-off [2,11]. Moreover, the scalings of radius, length and speed implied by (11) indicate that both curvature terms in (3) are indeed unimportant near pinch-off, not just the leading-order asymptotic term. Thus, pinch-off leads to an infinitely extended thread, as suggested numerically. Note that, in practice, this is not the final scaling prior to pinch-off because inertia eventually becomes important, and it is anticipated that the final pinch-off dynamics then takes a universal form (see part I).

3.1.3. Parameter variations

Given the final state, we define several terms for descriptive convenience in the discussion below; see Fig. 2e. The *final length* denotes  $|L(t)|$  at the time when  $h_{\min} = 0.05$ , and the *pinch-point* is the location of the minimum radius. The *neck* is the thinning region, defined as the length of the contiguous section having  $h < 0.1$  and containing the pinch-point. The *end-cones* bracket the neck.

Profiles of threads close to pinch-off for several values of  $\beta$  are shown in Fig. 3. For small yield stress, surface tension pulls the drop into a more spherical shape, whereas for large  $\beta$  a substantial rigid tube remains. With increasing  $\beta$ , the neck shortens, the end-cones become more squat, and the position of the pinch-point rises, all due to the extra mass accommodated in the pendant drop for bigger yield stress (the final length has a more complicated dependence on  $\beta$ ). The increase of the drop volume with  $\beta$  roughly matches the simple approximation,  $(\sqrt{3}\beta + 1)\pi/G$ ; the error in this estimate is shown in Fig. 3g, along with data from the full analytic prediction (9). At this value of  $\mathcal{W}$ , the simple approximation gives a relative error of about 65% at small  $\beta$  and improves to 5% at large  $\beta$  (where the thinning is rapid compared to extrusion once the pinching regions yield, see Fig. 3f).

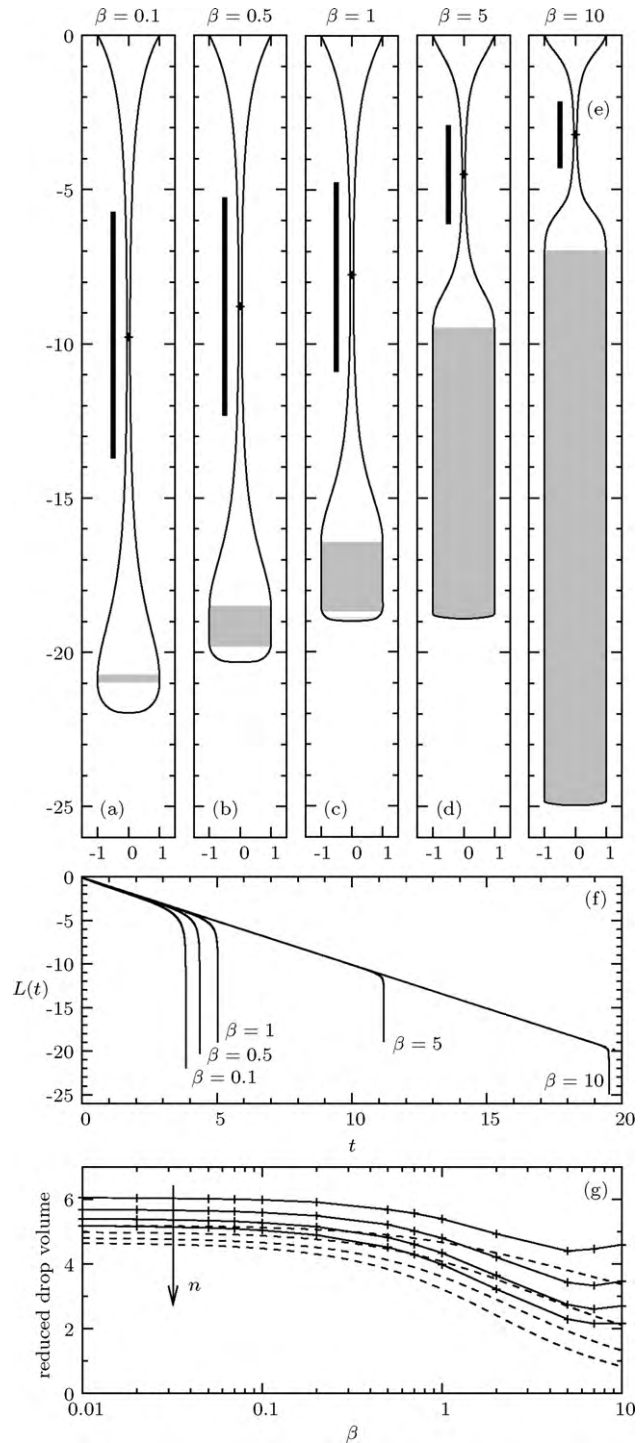


**Fig. 3.** Inertialless drops with various yield-stress parameters for  $\mathcal{W} = G = 1$  and  $n = 0.6$ . (a–e) Final profiles; shaded regions are unyielded, + indicates the location of the pinch-point and the bold line indicates the neck region; this convention is also used in later figures. (f) Position of base of drop against time (solid curves). The  $L(t)$  curves overlap along the inclined straight section  $-0.1 - \mathcal{W}t$ . (g) Drop volume less  $(\sqrt{3}\beta + 1)\pi/G$  against  $\beta$  for  $n = 0.2, 0.4, 0.6$  and  $0.8$ . Solid curves with symbols are the numerical solutions; dashed curves are the analytic predictions derived from (9). ( $N = 200$ .)

Thread profiles with changing power-law exponent are shown in Fig. 4. Proceeding right to left from weak to strong shear thinning, the neck shortens substantially, the end-cones become more squat, the final length decreases and the drop volume increases. These all result from a decreasing resistance to stretching in the highly stressed neck prior to pinch-off.

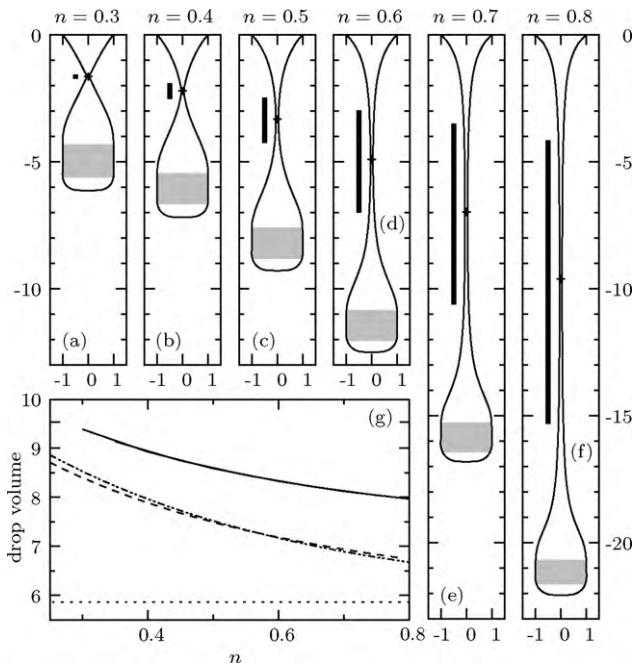


**Fig. 4.** Inertial drops with various power-law exponents for  $\mathcal{W} = 0.1$ ,  $G = 1$  and  $\beta = 0.5$ . (a–f) Final profiles, decorated as in Fig. 3. (g) Drop volume against power-law exponent: the solid curve is numerical, the dashed curve is the analytic solution (9), the dotted line is the approximate solution  $(\sqrt{3}\beta + 1)\pi/G$  and the dash-dotted curve is (10). ( $N = 100$ .)

Drop volumes for varying extrusion speed are shown in Fig. 5. As  $\mathcal{W}$  increases, more fluid is extruded before pinch-off occurs, increasing the drop volume. Simultaneously, since surface tension plays less of a role during the pinch-off, the end-cones elongate, the neck lengthens, the pinch-point is lowered and the final length increases (see the sample pair of profiles also pictured). In Fig. 5 the analytic approximation (9) to the drop volume compares well with the numerical computation for the entire range of  $\mathcal{W}$  shown. This figure, along with Figs. 3g and 4g, allows us to gauge the usefulness of the analytical expressions for the drop volume, on which we base some results regarding rheometry in the conclusions. Overall, the explicit approximation in (10) is almost as accurate as the implicit

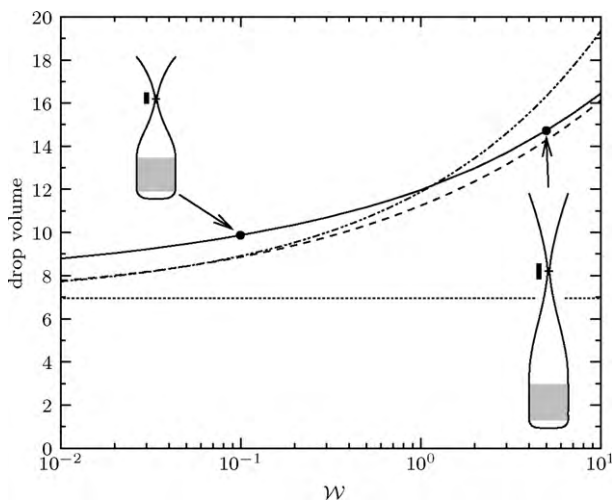


**Fig. 5.** Inertial drop volume against extrusion speed for  $G = 1$ ,  $\beta = 0.7$  and  $n = 0.4$ . The solid curve is the full numerical solution, the dashed curve is the analytic solution (9), the dotted line is the approximate solution  $(\sqrt{3}\beta + 1)\pi/G$  and the dash-dotted curve is (10). Profiles are shown at  $\mathcal{W} = 0.1$  and  $\mathcal{W} = 5$ , decorated as in Fig. 3. ( $N = 100$ .)

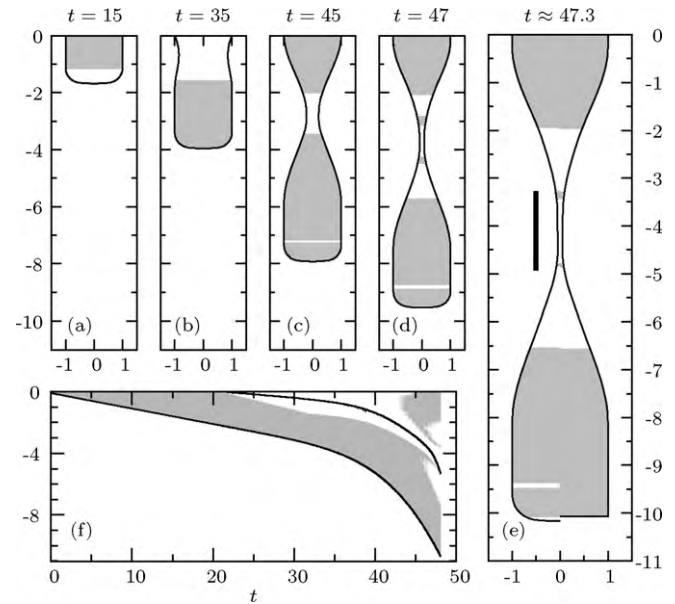


**Fig. 6.** Inertial Bingham ( $n = 1$ ) drop for  $\mathcal{W} = 0.1$ ,  $G = 1$ ,  $\mathcal{R} = 10$  and  $\beta = 0.7$ . (a–e) Profiles at different times. In (e), the right-hand-side shows the free-tip solution. (f) Position of base of drop, unyielded region (shaded) and minimum radius location against time for the free-tip solution. ( $N = 200$  for profiles,  $N = 400$  for the right-hand-side of (e) and (f).)

expression (9), and in practical situations probably proves more useful owing to its simplicity.

### 3.2. Inertial drips ( $\mathcal{R} > 0$ )

A sample numerical solution with inertia is displayed in Fig. 6. At early times, the profiles are similar to inertialess ones: an unyielded plug is extruded until sufficient weight hangs below the orifice to yield the fluid and initiate thinning. However, as the drop falls away, because of inertia the gravitational stress is not fully balanced against internal stresses. Thus  $\tau_{zz}$  falls below the yield value and a new unyielded plug is generated at the orifice. Close to pinch-off, unyielded plugs also form in the neck around the locations where the stress switches from tensile (in the narrowest regions) to compressive (in the end-cones). As the evolution proceeds to pinch-off these plugs become increasingly narrow and inconsequential, as found in part I for the Rayleigh instability. As expected, pinch-off now appears to be obtained at finite length (compare Figs. 2g and 6f). We anticipate that the behaviour in the approach to pinch-off becomes self-similar, dictated by a balance between surface tension, inertia and viscous forces (see part I), but we did not confirm this numerically.

A sequence of profiles illustrating the effect of increasing  $\mathcal{R}$  for different values of  $\beta$  are shown in Fig. 7. For  $\mathcal{R} = 1$ , the solutions are similar to their inertialess counterparts, although the pattern of interlaced yielded regions and plugs is more complicated. For larger  $\mathcal{R}$ , the increased fluid inertia delays the adjustment of the new fluid emerging from the pipe, leading to more cylindrical upper sections, and the pinching of the lower sections, to generate drops with greater volume. The neck also becomes shorter and increasingly asymmetrical, with the pinch-point occurring closer to the actual drop (as for Newtonian fluids).

At fixed  $\mathcal{R}$ , increasing the extrusion speed also promotes inertial effects because of the increase in the dimensionless velocities. In fact, for sufficiently large  $\mathcal{W}$  with  $\mathcal{R} > 0$ , the inertia delays thinning sufficiently that a secondary region of thinning appears above the primary one; see Fig. 8. At yet higher  $\mathcal{W}$ , we anticipate that multiple interlaced plugs and thinning regions can appear, although

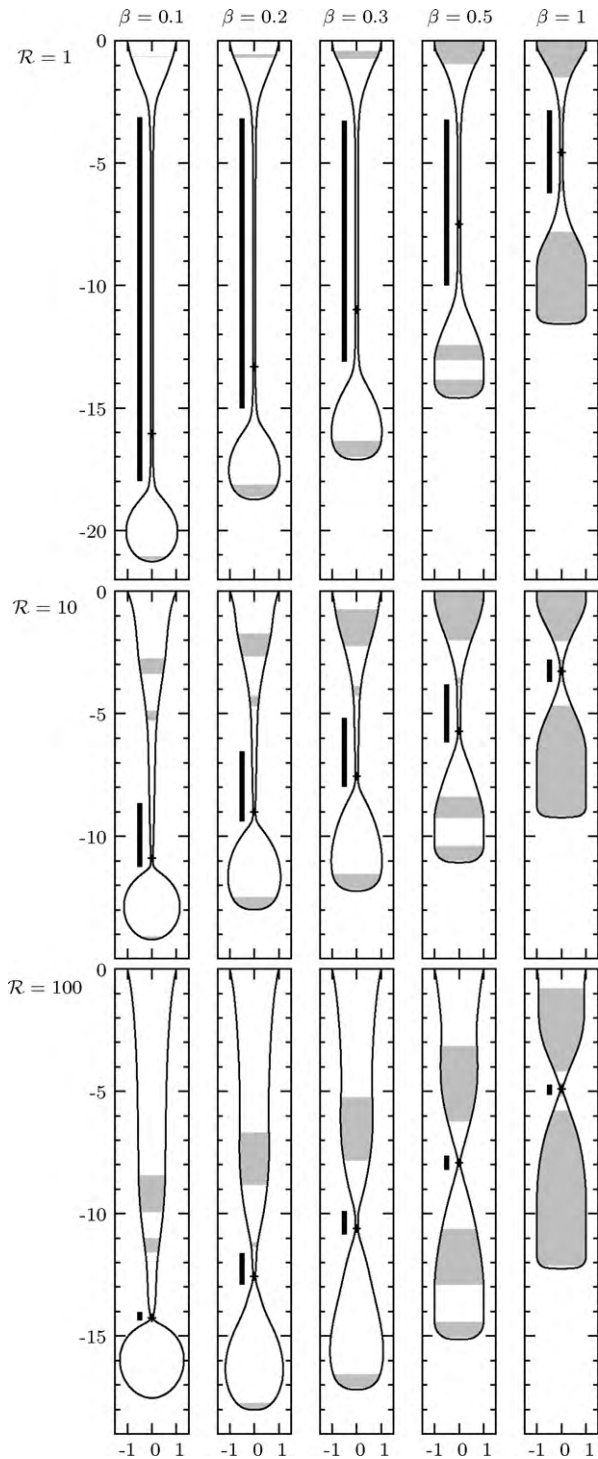


**Fig. 7.** Inertial drop profiles at  $h_{\min} = 0.05$  for Bingham fluids ( $n = 1$ ) with  $G = 1$  and  $W = 0.1$ . Rows correspond to (a)  $R = 1$ , (b)  $R = 10$  and (c)  $R = 100$ . Columns correspond to (i)  $\beta = 0.1$ , (ii)  $\beta = 0.2$ , (iii)  $\beta = 0.3$ , (iv)  $\beta = 0.5$  and (v)  $\beta = 1$ . ( $N = 200$ .)

we have not been able to show this numerically. The behaviour appears to be analogous to the “string of sausages” regime observed experimentally by Coussot and Gaulard [8].

### 3.3. Experiments

Our dripping experiments were performed by driving either a Carbopol solution or a Kaolin slurry through vertical pipes of vary-

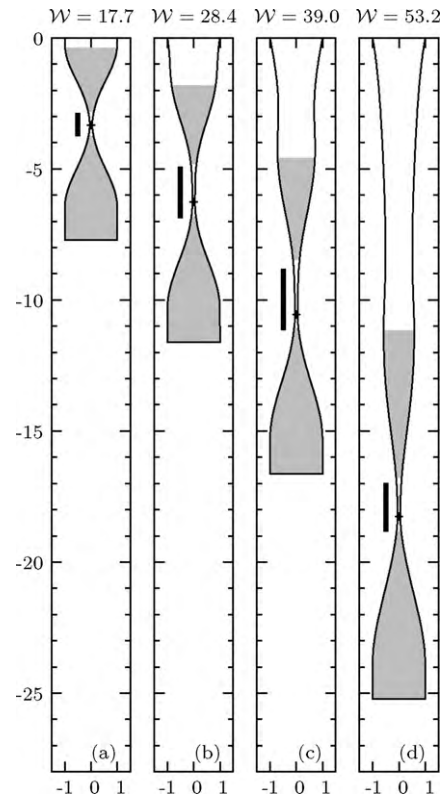


**Fig. 8.** Inertial drop profiles with  $h_{\min} = 0.05$  for various extrusion speeds with  $R = 1.49 \times 10^{-3}$ ,  $G = 5.85$ ,  $\beta = 3.35$  and  $n = 0.43$ , corresponding to Carbopol experiments with our wider pipe in Section 3.3. Shaded regions are unyielded. ( $N = 200$ ; boundary conditions (6).)

ing radii. The fluids were fed from a reservoir in a cylinder fitted with a piston attached to a computer-controlled linear actuator. The setup effectively duplicated a standard syringe pump, although the volume capacity and range of flow rates were much larger. Images of the pinching threads were taken with a high speed CMOS camera (Mikrotron EoSens CL); by using various lenses and only a fraction of the total pixels, we were able to obtain up to 10,000 fps with a spatial resolution of 0.042 mm/pixel. Extrusion rates ranged from 0.059 to 39.3 mL/s, and were measured with an accuracy of  $\pm 0.5\%$ . Two different pipe radii, 3.3 and 6.6 mm, were used.

Stress versus shear-rate curves for the two fluids in steady shear were measured using a Bohlin CS rotational rheometer; Appendix B summarizes the detailed properties of the fluids, together with fits of the rheometric data to the Herschel–Bulkley model. The Herschel–Bulkley parameter values are given in Table 1. Table 2 lists the relevant dimensionless parameters for the different experimental configurations considered, assuming both materials had the same surface tension as water (direct measurements of this quantity were unavailable).

A sequence of images from a sample Carbopol experiment are shown in Fig. 9, with overlaid theoretical profiles. Note that the

**Table 1**

The rheological parameters determined from fitting the stress–shear-rate curves to the Herschel–Bulkley model or fitting the drop volumes to (10).

|                        | $\tau_y/\text{Pa}$ | $K/\text{Pa s}^n$ | $n$   |
|------------------------|--------------------|-------------------|-------|
| Carbopol – up ramp     | 37                 | 13.6              | 0.429 |
| Carbopol – down ramp   | 28                 | 15.8              | 0.411 |
| Carbopol – drop volume | 42                 | 8.6               | 0.488 |
| Kaolin – up ramp       | 228                | 10.4              | 0.483 |
| Kaolin – down ramp     | 246                | 0.128             | 1.21  |
| Kaolin – drop volume   | 157                | 10.5              | 0.634 |

**Table 2**  
Dimensionless parameter values for the different experimental configurations.

| Fluid    | R/mm | $\mathcal{R}$         | $G$  | $\beta$ | $n$  | $\mathcal{W}$ |
|----------|------|-----------------------|------|---------|------|---------------|
| Carbopol | 3.3  | $4.69 \times 10^{-3}$ | 1.46 | 1.68    | 0.43 | 0.226–5.65    |
| Kaolin   | 3.3  | $1.78 \times 10^{-2}$ | 2.30 | 10.3    | 0.48 | 0.145–14.5    |
| Carbopol | 6.6  | $1.49 \times 10^{-3}$ | 5.85 | 3.35    | 0.43 | 0.142–71.0    |
| Kaolin   | 6.6  | $7.97 \times 10^{-3}$ | 9.21 | 20.7    | 0.48 | 0.077–30.9    |

experimental drip continues from a previous pinch-off, whereas the theory employs the free-tip boundary condition (6), so the two cannot be compared at the bottom of the drop. Nevertheless, the theoretical predictions are in reasonable agreement for the qualitative shape in the overlying thinning region. Other details compare less favourably, however: a substantially longer neck is observed experimentally. This discrepancy could indicate that our Herschel–Bulkley fit provides too low a value for  $n$  at large extensional stresses. Indeed, the rheological data is not especially well fit by a single power law over the entire range of stresses (see Appendix B).

More dramatically, once the neck became very long and thin, secondary pinches could form that broke this thinned region into satellite drops. Satellite formation was irregular and unrepeatable, reflecting the importance of noisy variations, much as has been observed for high viscosity Newtonian fluids. For viscous fluids, surface tension subsequently pulls the satellites into spherical shapes. With our yield-stress fluids, some recoil (due either to surface tension or fluid elasticity or both) was evident and the droplets typically contracted into slender ellipsoids rather than spheres.

Images of a Kaolin drip are shown in Fig. 10, again with overlaid theoretical profiles. For this material, the experiment compares poorly with theory. One possible source of the disagreement could be our adoption of the surface tension of water for the Kaolin suspension. However, if we try and “calibrate” the surface tension of the suspension by matching numerical profiles to the experiments, the comparison is only improved if the surface tension is made 10 or 20 times larger than that of water. More likely is that the consti-

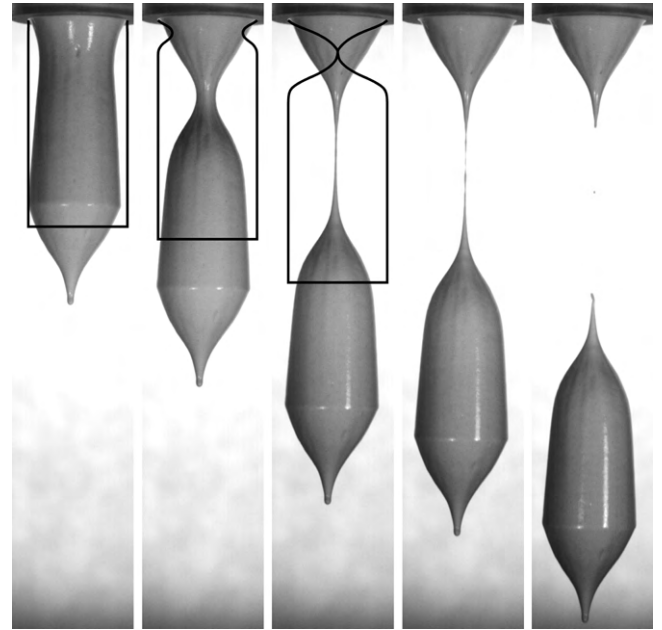


**Fig. 10.** Experimental and numerical profiles for Kaolin with a 6.6 mm radius pipe and  $\mathcal{W} = 0.0802$ . (Frames 1, 1413, 1473, 1484 and 1510 at 1663 fps.) ( $N = 100$ ; boundary conditions (6); pinch-off time matched.)

tutive behaviour of Kaolin is poorly fit with the Herschel–Bulkley model, as suggested by other attempts to match theory with unsteady experimental flows [5] and apparent thixotropy in our rheometry (see Appendix B and Fig. 21). For example, the experimental behaviour evident in Fig. 10 suggests deformation may be occurring below the measured yield stress.

A comparison of observed and predicted drop volumes for both materials is shown in Fig. 11. Also included in the figure are Coussot and Gaulard’s data from their experiments with a commercial hair gel, as well as their theoretical result (which is identical to

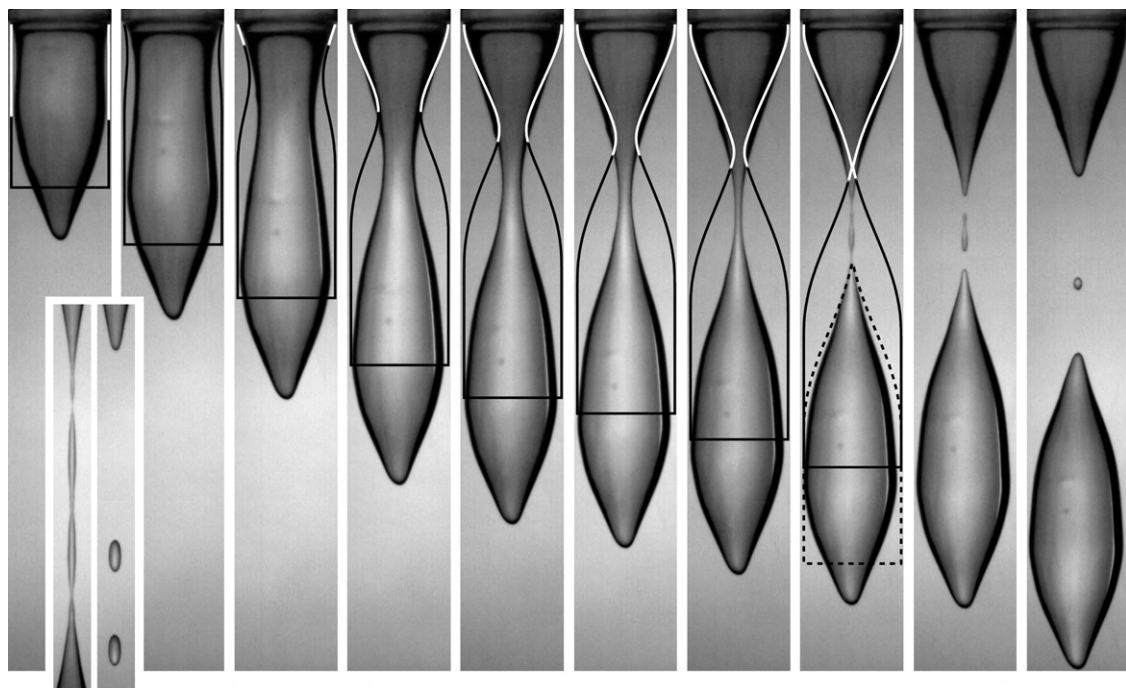


**Fig. 9.** Experimental profiles for Carbopol with a 3.3 mm radius pipe and  $\mathcal{W} = 2.35$ . (Frames 0, 300, 450, 520, 540, 550, 560, 570, 571 and 588 at 1970 fps.) The superimposed black and white (for contrast) curves are corresponding numerical profiles. The dashed curves are the pinched-off drop profile translated to coincide with the top of the experimental drop. ( $N = 200$ ; boundary conditions (6); pinch-off time matched.) The inset shows the formation of ellipsoidal satellites at  $\mathcal{W} = 5.88$  at same scale.



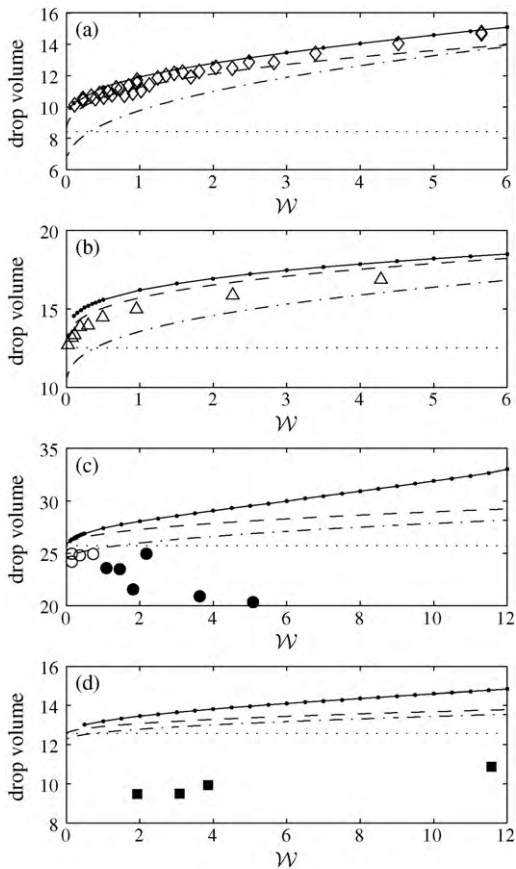


**Fig. 11.** Dimensionless drop volumes as a function of  $\mathcal{W}$ . Symbols correspond to experiments (open are direct measurements of drop mass, solid are taken from the time interval between pinch-off events). The solid curves (with points) correspond to numerical solutions with inertia, the dashed curves to the analytic prediction in (9), the dash-dotted to Coussot and Gaulard's theoretical result (no surface tension) and the dotted lines to the leading-order estimate  $(\sqrt{3}\beta + 1)\pi/G$ . Symbols: (a)  $\diamond$  correspond to Carbopol with a 3.3 mm radius pipe; (b)  $\triangle$  to Coussot and Gaulard's gel ( $\mathcal{R} = 1.34 \times 10^{-5}$ ,  $G = 1.20$ ,  $\beta = 2.18$ ,  $n = 0.355$ ); (c)  $\circ$  to Kaolin with a 3.3 mm radius pipe; (d)  $\square$  to Kaolin with a 6.6 mm radius pipe. ( $N = 100$ ; boundary conditions (6).)

(10) with the surface tension term removed [8]). For the Carbopol solutions, the numerical results compare favourably with experiment, although they slightly over-predict the true volumes. The comparison is even tolerable for Kaolin at small  $\mathcal{W}$ . When  $\beta \gg 1$  the drop volume is predominantly determined by the yield stress and the simple approximation  $z_{0p} = (\sqrt{3}\beta + 1)\pi/G$  proves quite accurate; surface tension and the extrusion speed have little effect (e.g., the Kaolin with a 6.6 mm radius pipe). However, when  $\beta \sim O(1)$  all the physical parameters provide a distinct contribution to the drop volume. (The effect of surface tension can be seen by comparing our analytical prediction with the theoretical result of Coussot and Gaulard in Fig. 11.)

We were also able to observe Coussot and Gaulard's "sausage-on-a-string" regime in the experiments. Images of Carbopol threads with different numbers of "sausages" are shown in Fig. 12. The number of distinct, connected thinning regions varied with the extrusion speed, as shown in Fig. 12e. The extrusion speed for which the second thinning region appears ( $\mathcal{W} \approx 18$ ) compares well with the theoretical results displayed in Fig. 8.

#### 4. Viscoplastic bridges

We next consider the extension of a filament attached to plates that are pulled outwards with a controlled displacement (see

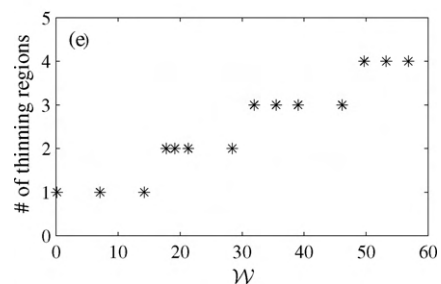
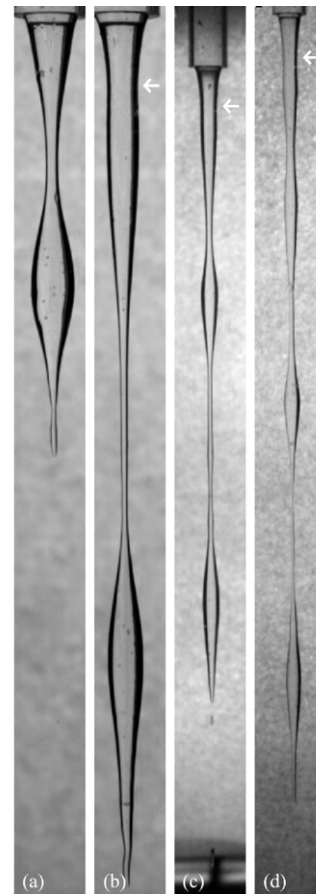


**Fig. 12.** Images of the fluid thread showing an increasing number of distinct thinning regions. The images are from experiments using Carbopol with the 6.6 mm radius pipe (a)  $\mathcal{W} = 17.7$ , (b)  $\mathcal{W} = 28.4$ , (c)  $\mathcal{W} = 39.0$ , (d)  $\mathcal{W} = 53.2$ . (e) The number of distinct thinning regions observed in experiments as a function of  $\mathcal{W}$  for the same fluid and pipe.

Fig. 1b), assuming the fluid to be pinned to the outer edge of the plates by surface tension. This protocol specifies the rate of extension rather than the extensional force (as in the drip problem). Specifically, we consider the case where the lower plate is held fixed but the top plate is pulled upwards at constant velocity, implying the boundary conditions,  $h(0, t) = h(L, t) = 1$ ,  $w(0, t) = 0$  and  $w(L, t) = \mathcal{W}$ , where  $L(t) = L_0 + \mathcal{W}t$  is the (prescribed) position of the top plate, and  $L_0$  is its initial location. Computations begin with a stationary cylinder,  $h(z, 0) = 1$  and  $w(z, 0) = 0$  for  $0 \leq z \leq L_0$ , and we integrate (1) and (2) numerically until the minimum radius  $h_{\min} = 10^{-3}$ .

The initial aspect ratio  $L_0$  adds a new parameter, which makes explorations of the parameter space somewhat unwieldy. To expedite the study, we therefore consider purely inertialess filaments, although we did perform computations including inertia to verify that its effect was not overly significant for values of  $\mathcal{R}$  that were not large.

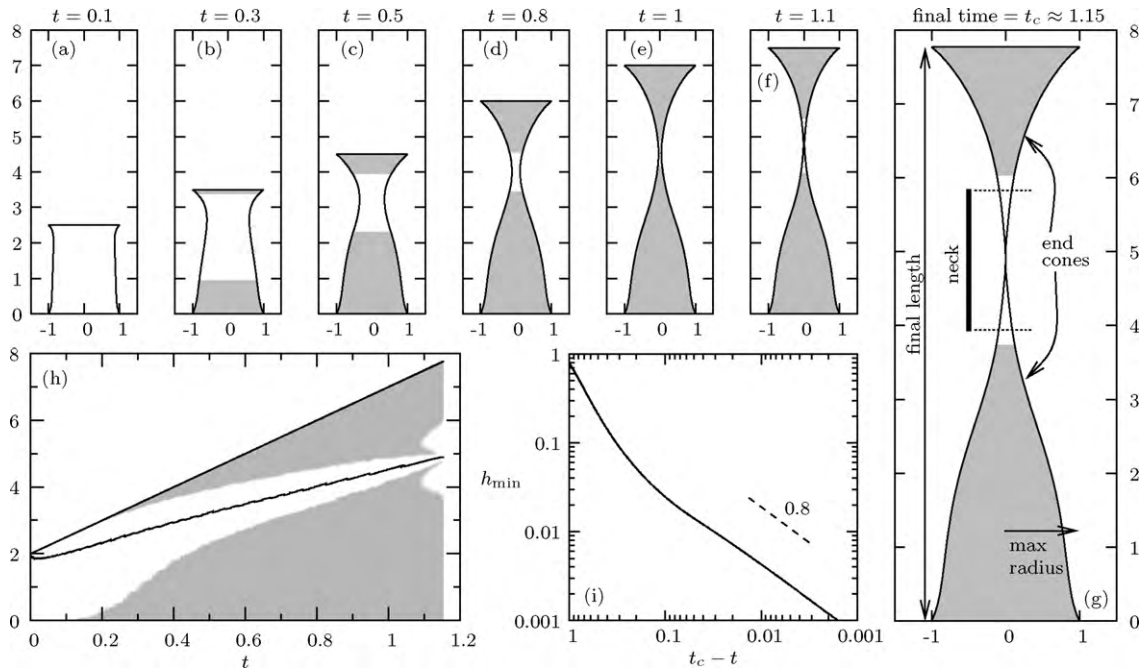


**Fig. 13.** Inertialess bridge problem with  $\mathcal{W} = 5$ ,  $G = 1$ ,  $\beta = 5$ ,  $n = 0.8$  and  $L_0 = 2$ . (a–g) Profiles at various times; shaded regions are unyielded and the bold line indicates the neck region (a convention we again adopt in subsequent figures). (h) Location of the top plate, unyielded regions and location of minimum radius against time. (i) Minimum radius against time. The expected slope near pinch-off  $(t_c - t)^n$  is indicated by the dashed line. ( $N = 100$ .)

#### 4.1. Inertialess bridges ( $\mathcal{R} = 0$ , $\mathcal{W}$ finite)

A sample numerical solution is shown in Fig. 13. Initially the stress induced by the sudden extension is sufficient to liquefy and thin the entire column, with gravity causing material to slump downwards slightly. As the thread thins, the extensional force required to maintain the velocity of the upper plate decreases and the stress eventually drops below the yield stress in the thickest regions, forming plugs adjacent to the end-plates which expand as the thread continues to thin. A more complicated flow pattern develops near the final pinch-off event: once the upward elongational force is sufficiently small, some regions yield again under the action of gravity and surface tension. Importantly, pinch-off appears to occur at a finite length (Fig. 13i). Just prior to pinch-off, the minimum radius converges to the self-similar scaling,  $h_{\min} \propto (t_c - t)^n$ , expected for a power-law fluid [12]. In other words, as observed with the Rayleigh instability, the yield stress plays a minor role in the final pinch-off dynamics.

##### 4.1.1. The initial yield

The initial stress state is a useful indicator of whether gravitational collapse will occur. In the sample evolution described above, the entire column initially yielded in extension. However, if  $G$  is large or the column is tall, gravity can counterbalance the extensional force near the base of the column, rendering that part of the filament rigid, or even force the fluid there to yield in compression as the material slumps under its own weight.

To determine the conditions under which the different situations occur, we first integrate the vertical momentum Eq. (2) to find

$$\frac{3}{2}h^2\tau_{zz} = -h - \int_z^L Gh^2 dz + f_0, \quad (12)$$

where the constant of integration,  $f_0 = 3\tau_{zz}(L, 0)/2 + 1 > 0$ , represents the force exerted on the top of the fluid column in order to move the upper plate. That force becomes known on imposing the velocity boundary condition,  $\mathcal{W} = w(L, 0) = \int_0^L (\partial w / \partial z) dz$ , leading

to the implicit relation,

$$\mathcal{W} = \int_{|\tau_{zz}| > 2\beta/\sqrt{3}} \frac{1}{\sqrt{3}} \left( \frac{\sqrt{3}}{2} |\tau_{zz}| - \beta \right)^{1/n} \text{sgn}(\tau_{zz}) dz, \quad (13)$$

where the integral is only over the yielded regions. By substituting the initial condition into (12), and then using (13), we may eliminate  $f_0$  to furnish  $\tau_{zz}(z, 0)$ , and then calculate the yield surfaces. The uppermost of these,  $z = z_Y$  (with  $\tau_{zz}(z_Y, 0) = 2\beta/\sqrt{3}$ ), is given implicitly by

$$\begin{aligned} (L_0 - z_Y)^{1+1/n} - [\max(0, z_Y - 2\sqrt{3}\beta/G)]^{1+1/n} - [\max(0, -z_Y)]^{1+1/n} \\ = 3^{(1+n)/2n} \left( 1 + \frac{1}{n} \right) G^{-1/n} \mathcal{W}. \end{aligned} \quad (14)$$

The switches on the left of this formula have the following interpretations: if  $z_Y < 0$ , the entire column is initially liquefied by the extensional stress; that is, the force exerted by the upper plate overcomes both the yield stress and gravity to extend the fluid bridge everywhere (as in Fig. 13). For  $0 < z_Y < 2\sqrt{3}\beta/G$ , on the other hand, the gravitational stress is sufficient to counter the extensional stress at the bottom of the column, forming a rigid plug underneath the yielded upper regions. Finally, when  $z_Y > 2\sqrt{3}\beta/G$ , gravitational compression liquefies the base of the column, and a rigid plug divides that yielded zone from the upper region of extension.

##### 4.1.2. Parameter variations

Again we define a number of helpful characteristic properties to assist the discussion: neck length, end-cone profiles, final length, pinch-point location (now measured relative to the bottom plate), and maximum radius (a measure of the degree of gravitational slumping). These quantities are illustrated in Fig. 13g.

Sample solutions with varying yield stress are shown in Fig. 14. The effect of  $\beta$  on the shape of the end-cones is particularly distinctive: for small  $\beta$ , surface tension rounds the cones in the final stages before pinch-off, creating more spherical shapes. Truly conical end-cones result at moderate  $\beta$  when the yield stress first arrests this behaviour. For large  $\beta$ , the bottom of the column never yields

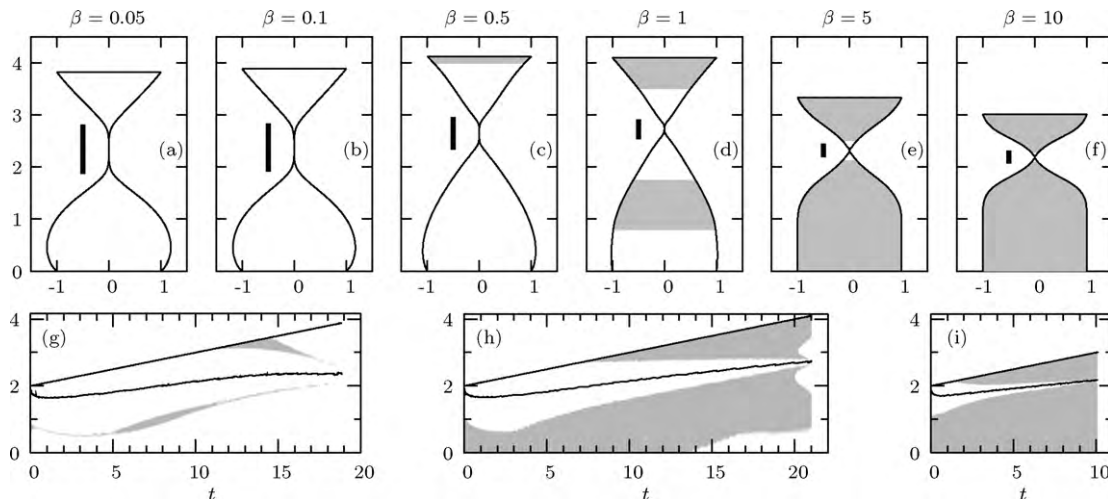


**Fig. 14.** Inertialless bridge problem with  $\mathcal{W} = 0.1$ ,  $G = 1$ ,  $n = 0.9$  and  $L_0 = 2$ . (a–f) Profiles at pinch-off for various yield-stress parameter values. (Bottom panels) Locations of the top plate, unyielded regions and minimum radius against time for (g)  $\beta = 0.1$ , (h)  $\beta = 1$  and (i)  $\beta = 10$ . The shaded regions are unyielded. ( $N = 100$ .)

and the remainder “freezes” quickly to produce prominent changes in surface gradient and end-cones shaped like “Hershey’s kisses”. Although it is not visible in the figure, there is an initial rigid mid-section for the computation with  $\beta = 0.1$ , whereas for those with  $\beta = 1$  and 10 the yield stress is sufficient to support a rigid lower plug. In other words, the three computations illustrate the other two scenarios for the initial yield mentioned above.

Effects of further parameter variations are shown in Figs. 15–17. The most distinctive trends observed with these parameter variations are as follows: the main effect of increasing  $n$  is to lengthen the neck (Fig. 15), as also found earlier for the drips and for bridges of power-law fluids [14,15] (at higher magnification than shown in the figure the filaments do not remain slender at the pinch-point for  $n = 0.2$  and 0.4, as expected from the inertialless power-law similarity solution [12]). With increasing extension speed (Fig. 16), a greater force acts at the top plate to drive the extension, and more of the column becomes and remains liquefied. As  $G$  increases (Fig. 17), gravitational slumping widens the base of the bridge and aids its

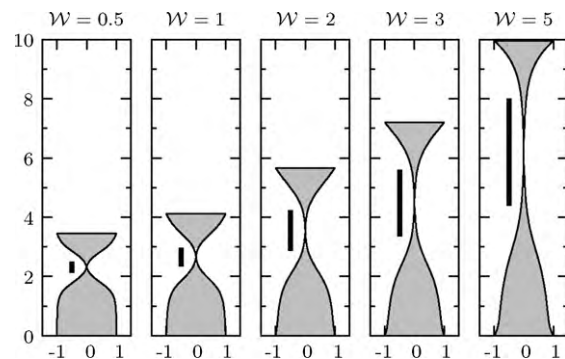


**Fig. 16.** Final profiles for various extension speeds for the inertialless bridge problem with  $G = 1$ ,  $\beta = 10$ ,  $n = 1$  and  $L_0 = 2$ . ( $N = 100$ .)

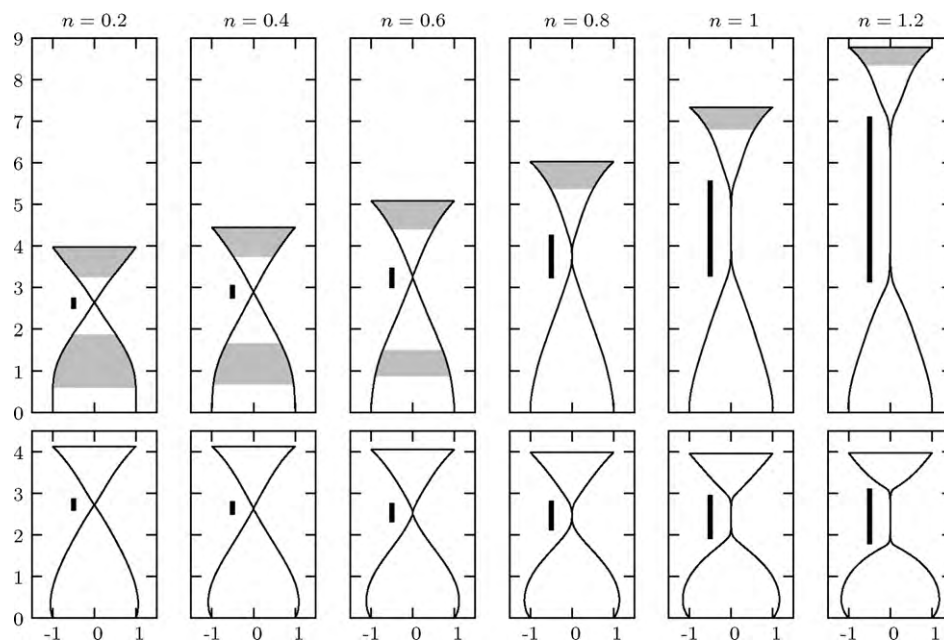


**Fig. 15.** Final profiles for various power-law exponents for the inertialless bridge problem with (top row)  $\mathcal{W} = G = \beta = 1$  and  $L_0 = 2$  and (bottom row)  $\mathcal{W} = 0.1$ ,  $G = 1$ ,  $\beta = 0.2$  and  $L_0 = 2$ . ( $N = 100$ .)

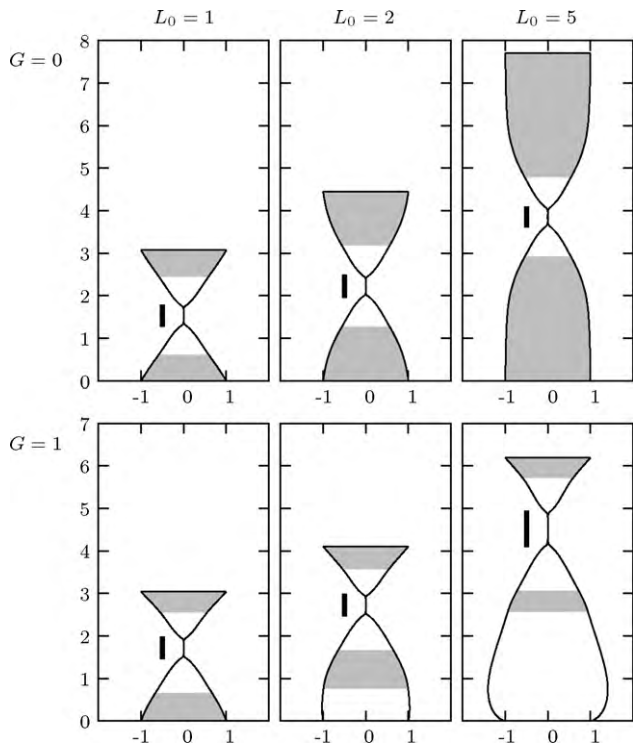


**Fig. 17.** Final profiles for various Bond numbers and aspect ratios for the inertialess bridge problem with  $\mathcal{W} = 0.1$ ,  $\beta = 1$ ,  $n = 1.2$ , (rows)  $G = 0$  and  $G = 1$ , and (columns)  $L_0 = 1$ ,  $L_0 = 2$  and  $L_0 = 5$ . ( $N = 100$ .)

thinning, leading to a shorter limiting length and a higher pinch-point. Varying the aspect ratio has a relatively minor effect (Fig. 17), suggesting  $L_0$  is not a useful parameter.

Overall, we find that the final time (or equivalently final length) is a convenient diagnostic for the rheological parameters. Contour plots of this quantity for  $\mathcal{W} = 0.1$  and 5 are shown in Fig. 18a and b. For small  $\mathcal{W}$ , a dominant and discernible trend is with  $\beta$ , while for large  $\mathcal{W}$ , the trend with the power-law exponent is more notable. This results because the yield stress is less important when the extensional force is large, and suggests that slow extension experiments may be useful for inferring the yield stress, whereas subsequent faster extensions could be used to infer the power-law

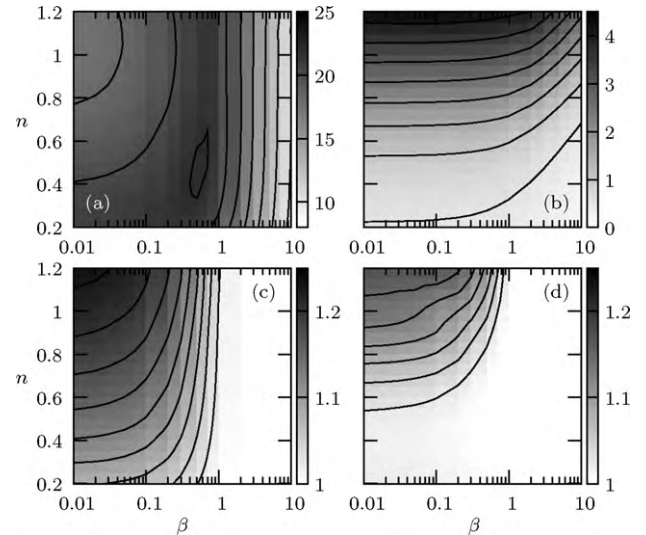


**Fig. 18.** Final time (top row) and maximum radius (bottom row) for inertialess bridges at pinch-off as densities on the  $(\beta, n)$  plane with  $G = 1$  and (left column)  $\mathcal{W} = 0.1$  or (right column)  $\mathcal{W} = 5$ . Contours at equal intervals of (a) 2 from 8, (b) 0.5 from 0 and (c,d) 0.025 from 1. ( $N = 100$ .)

exponent. A useful secondary diagnostic is the thread's maximum radius (Fig. 18c and d), which shows clear trends with both  $\beta$  and  $n$  (once the thread slumps under gravity).

#### 4.2. Experiments

The liquid bridge experiments were conducted using a HAAKE CaBER 1 extensional rheometer. Rather than using the rheometer's built-in laser measurement system (which only takes measurements at one fixed height), the extending bridges were again imaged using the CMOS camera. The rheometer plates were 3.0 mm in radius and were covered with a layer of waterproof sandpaper to prevent slip and dewetting. The top plate was moved upwards at speeds of 0.6–26 mm/s. Table 3 lists the relevant dimensionless parameters for the different experimental configurations.

Fig. 19 shows sequences of Carbopol threads with overlaid theoretical profiles at various times for two different aspect ratios and plate speeds. The theoretical profiles are for  $\mathcal{R} = 0$ , but there is no



**Fig. 19.** Experimental and numerical bridge profiles at various times for Carbopol with (top row)  $\mathcal{W} = 0.99$  and  $L_0 = 0.33$  and (bottom row)  $\mathcal{W} = 0.16$  and  $L_0 = 1.33$ . ( $N = 100$ .)

**Table 3**  
Non-dimensional parameter values for the different experimental bridge configurations. End-plates had a radius of 3 mm.

| Fluid    | $\mathcal{R}$         | $G$  | $\beta$ | $n$   | $\mathcal{W}$ | $L_0$      |
|----------|-----------------------|------|---------|-------|---------------|------------|
| Carbopol | $5.49 \times 10^{-3}$ | 1.21 | 1.52    | 0.429 | 0.0993–1.58   | 0.333–1.33 |
| Kaolin   | $1.99 \times 10^{-2}$ | 1.90 | 9.40    | 0.483 | 0.0480–0.960  | 0.333–1.33 |

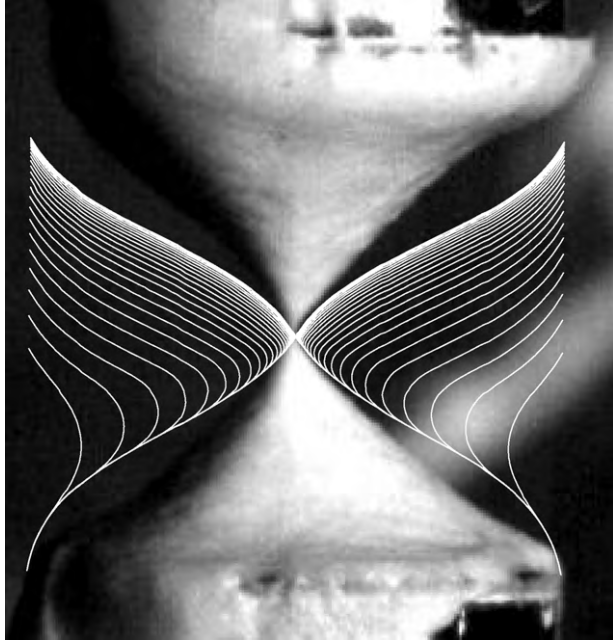


**Fig. 20.** Experimental bridge profile close to pinch-off for Kaolin with  $\mathcal{W} = 0.96$  and  $L_0 = 0.66$ . Curves show numerical profiles with minimum radii  $0.8^j$  for positive integer  $j$ . ( $N = 100$ .)

difference discernible on adding the actual small amount of inertia. The comparison is satisfactory for both sets, although thinning is a little too fast at early times and a little too slow closer to pinch-off. This is consistent with comparisons for the drips, and again suggests that our single power-law fit may not be a good representation over the range of stresses sampled by the flow.

The comparison of theory and experiment in Fig. 19 is especially remarkable given that the filaments are not particularly slender, which is the essential approximation underlying our theoretical model. Part of the reason behind this success may be the retention of the full curvature in (3), rather than the leading-order estimate,  $\kappa \sim 1/h$ , which is a standard trick for Newtonian filaments [1].

A similar sequence is shown for Kaolin in Fig. 20, with numerical calculations using the “up-ramp” rheological parameters (there is no appreciable difference if the “down-ramp” parameters are used, despite quite different numerical values and a much larger inertial parameter). The comparison is poorer, possibly because the thread is not slender, but again more likely because the Herschel–Bulkley model does not adequately describe the rheology.

**5. Conclusions**

In the two parts of the current work we have considered three canonical problems for the extensional dynamics of viscoplastic filaments. We began with the Rayleigh instability in paper I. We continued here with an investigation of the progression towards pinch-off of a pendant drop and the extension of an inertialess liquid bridge between two plates, comparing model predictions with experiments. For Carbopol, we found satisfactory agreement between observed and predicted drop volumes and bridge profiles, and reasonable agreement for drop profiles. Some minor differ-

ences can be attributed to the inadequacy of a single power-law to describe the fluid rheology over the full range of stresses. For Kaolin, theory and experiment do not agree; we suspect that this results from the Herschel–Bulkley model being a poor description for Kaolin rheology. In particular, we suspect that some deformation may be occurring at stresses below the yield value measured rheometrically and that the material is thixotropic.

Of particular interest are diagnostics that can be used to infer rheological properties. For drips, we found that the pinched-off drop volume is a useful diagnostic, in part because analytical estimates are available. The simplest available expression for the drop volume,  $V$ , is that obtained from (10), the dimensional version of which is

$$V = \pi R^2 z_{0Y} + \frac{\pi \sqrt{3} R^2 K}{\rho g} \left( \frac{\sqrt{3} W}{z_{0Y}} \right)^n, \tag{15}$$

where  $z_{0Y} = (\sqrt{3} \tau_Y + \gamma/R)/\rho g$ . For experimental arrangements like that used in the present study, Eq. (15) can be used to infer rheological properties. The dimensional version of the implicit analytic prediction in (9) or full numerical solutions could also be used, although it is not clear whether the implied improvement would be worth the extra effort.

For example, with a fixed geometry, and assuming that the surface tension is known, one may measure drop volumes over a range of extrusion speeds,  $W$ , and then perform a least-squares fit of the data to (15) to obtain estimates of  $K$ ,  $n$  and  $\tau_Y$ . To judge how well such a procedure might work, we performed such a fit using the data shown in Fig. 11 and again assuming that the surface tension was equal to that for water. The fitted rheological parameters are listed in Table 1 along with the values independently measured with a rheometer. For the Carbopol, while the fitted values seem to differ, the resulting stress-strain-rate curve is practically indistinguishable from the marker points shown in Fig. 21a. With Kaolin,

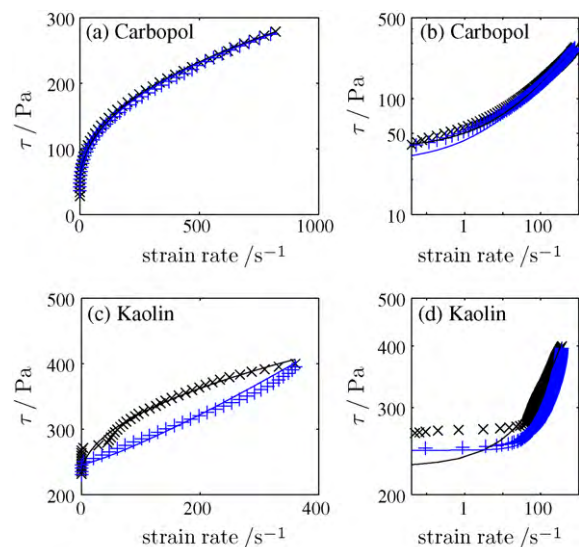


**Fig. 21.** The up ( $\times$ ) and down ( $+$ ) stress ramp curves for the Carbopol solution, (a) linear scale, (b) logarithmic scale; and the Kaolin suspension, (c) linear scale, (d) logarithmic scale (the same data is shown on both sets of axes). The Herschel–Bulkley fits corresponding to the parameters in Table 1 are given by the solid lines.

the new fit leads to computed drip and bridge profiles that compare better with experiments, but the overall agreement is still poor.

A problem with (15) is that the surface tension and yield stress only appear via the combination  $z_0\gamma$ . Thus, if neither are known, the radius of the pipe,  $R$ , must be varied in order to fit both constants. Alternatively, if the rheological data is available independently, the least-squares fit can be used to infer the surface tension. To gauge this procedure we use the data in Fig. 11 in conjunction with the up-ramp measurements listed in Table 1 to arrive at a surface tension of 0.060 N/m for Carbopol, in comparison to the previously adopted value of 0.073 N/m, suitable for water at room temperature. Although we are currently unable to confirm this reduction in surface tension, it is not unreasonable. Using this value of  $\gamma$  does not perceptibly change, for example, the predicted profiles in Fig. 9.

To infer rheology using the bridge, we found that the time for pinch-off for a liquid bridge is a useful diagnostic. In the quasi-static limit, this diagnostic could provide estimates for yield stress, while for faster flows it can be used to infer the power-law exponent. A disadvantage is that pinch-off time is not given analytically in the model, and requires extraction from suites of numerical computations. Nevertheless, in the inertialess limit, computations are relatively fast (for  $N = 100$ , each run takes a few minutes), which opens the door to using a real-time parameter search to optimally match a numerical profile to experiments. Because the bridge samples a large range of extension rates, a few experiments may be sufficient to provide estimates of the three rheological parameters  $K$ ,  $n$  and  $\tau_Y$ , as well as the surface tension coefficient  $\gamma$ .

We emphasize that this approach to using the bridge as a rheometer is more practical for viscoplastic fluids than conventional usage. For the latter, the initial column of fluid is stretched a specified distance. Once this distance is reached, the thickness of the thread at a fixed point is measured and its radius over time is recorded. Rheological parameters can then be calculated from the rate at which the thread thins. For a viscoplastic fluid, however, it is difficult to set the displacement of the plates so that the material does not pinch-off while the plates are still moving or to prevent the yield stress from “freezing” all the material into place once the plates come to rest. Moreover, we found that long, thin threads generally do not occur for viscoplastic fluids (see Section 4.2), as a result of both their generally shear-thinning nature and the yield stress.

Finally, although we adopted the Herschel–Bulkley model, there is plenty of scope to attempt rheometry using different constitutive laws. The slender filament approximation potentially offers useful simplification of more complicated models, and fitting procedures of the kind described here ought to furnish convenient calibrations. Admittedly, however, we rely on an explicit form for the constitutive law and offer no direct inference of extensional rheology.

## Appendix A. Numerical scheme

We solve the model equations by discretizing in space using the staggered-mesh finite-difference approximation suggested by Eggers and Dupont [16], introducing a moving spatial grid to deal with the evolving domain and to resolve the regions with high curvature. We integrate the resulting ODEs in time using DASPK [17]. The variables  $h$  and  $\tau_{zz}$  are defined on an evolving principal mesh of  $N + 1$  grid points  $z_i(t)$  for  $i = 1, \dots, N + 1$ , and  $w$  is defined on the half-node mesh of  $N$  grid points at  $z_{i+1/2}(t) = [z_i(t) + z_{i+1}(t)]/2$ . A 3-point stencil is used to find  $\kappa$  on principal grid points, except at the first eight grid points for the drops with a spherical-cap initial condition. There we evaluate the curvature using an even 4th order polynomial interpolation through  $z(h)$  [16]. We also evaluate  $\Gamma \equiv \partial w / \partial z$  at the principal nodes from  $\tau_{zz}$  via (4). To deal with the non-smooth switches in the constitutive relation, we either approximate the implied Heaviside function  $H(x)$  by  $H(x) =$

$(1 + x / \sqrt{x^2 + \epsilon^2})/2$ , with  $\epsilon = 10^{-5}$ , or use the root-finding capability of DASPK (DASKR) to find the transition between yielded and unyielded states. Sample solutions computed using the two methods are visually indistinguishable, as are regularized solutions computed with  $\epsilon = 10^{-4}$ .

Eq. (1) is applied at the interior principal grid points using a 3-point stencil, with  $\Gamma$  substituting for  $\partial w / \partial z$ . For inertialess problems, we impose (2) at the half-node grid points using a 2-point stencil. For problems with inertia, we found it better to use  $\Gamma$  as the dependent variable, applying

$$\mathcal{R} \left( \frac{\partial \Gamma}{\partial t} + w \frac{\partial \Gamma}{\partial z} + \Gamma^2 \right) = - \frac{\partial^2 \kappa}{\partial z^2} + \frac{\partial}{\partial z} \left[ \frac{3}{2h^2} \frac{\partial}{\partial z} (h^2 \tau_{zz}) \right]$$

at the interior principal grid points using a 3-point stencil. At the top point,  $z_{N+1}$ ,  $\partial w / \partial t = 0$  and  $w$  is given, thus we impose (2) directly. We recover  $w$  at interior principal grid points using a 2-point stencil. For drips with the spherical-cap initial condition, the value of  $\tau_{zz}$  at  $z_1(t)$  is irrelevant provided it is finite and we set it to zero.

For the drips we use the dynamically moving mesh method of Blom and Zegeling [18]; the scaled grid points  $z_i(t)/z_1(t)$  are redistributed according to the monitor function  $M(z) = (1 + (\partial h / \partial z)^2 / \max(\partial h / \partial z)^2 + 0.5\kappa / \max(\kappa))^{1/2}$ . The algorithm parameters used were  $\kappa_{BZ} = 2$  and  $\tau_{ZB} = 0.002$ . The first 2 grid points are moved with the local fluid velocity. For the bridge we use Lagrangian coordinates, moving all grid points with the local fluid velocity. After  $N$  time steps, we invoke a static remeshing, evenly distributing the monitor function  $M(z) = (0.1 + (\partial h / \partial z)^2 / \max(\partial h / \partial z)^2 + \min(h)/h)^{1/2}$  between grid points and interpolating onto the new grid using a quintic spline for  $h$  and a cubic for  $\tau_{zz}$  (and  $w$  for the inertial case). Both choices of monitor function concentrate grid points in regions of high curvature and large gradients in  $h$ .

The numerical computations are considerably more expensive than for the corresponding Newtonian problems, limiting the achievable number of grid points. The profiles presented in the main text change imperceptibly on increasing  $N$ . For the drips with the spherical cap initial condition, round-off errors accumulate near the base of very long plug regions leading to oscillations in the stress after many time steps. Fortunately this is not a severe problem for the profiles presented: the location of the plug and details of the solution above the plug are identical to the corresponding solution using (6), which suffers no such problems.

## Appendix B. Experimental fluid properties

The Carbopol solution was a 0.18 wt% Carbopol Ultrez 21 solution neutralized with sodium hydroxide to a pH of 7.0. The Kaolin suspension was a 40.8/59.0/0.2 wt% mixture of water/Kaolin/sodium hydroxide. The Kaolin clay used was Mcnamee Clay provided by R.T. Vanderbilt Co. Inc. The pH of the suspension was 12.5; (the pH was increased to reduce the amount of separation that occurs when the suspension is left to sit for long periods of time). The densities of the Carbopol solution and Kaolin suspension were 1000 and 1570 kg/m<sup>3</sup>, respectively. In the absence of existing reliable measurements, we assume a surface tension equal to that of water, 0.0728 N/m, for both the Carbopol solution (cf., [19]) and the Kaolin suspension.

The rheology of the two fluids was measured using a Bohlin CS rotational rheometer with a plate-plate geometry. Both plates were serrated in order to avoid possible slip at the surface. Increasing and decreasing controlled-stress rheometry tests were done (the “up” and “down” ramps respectively). For each of the ramps the stress was increased/decreased continuously over the desired range at a rate of 1 Pa/s for the Carbopol and 0.5 Pa/s for the Kaolin.

The fluid parameters were determined by fitting the stress-strain-rate curves obtained to the Herschel–Bulkley constitutive model. Typical stress-strain-rate curves for the two fluids are shown in Fig. 21 and the values of the rheological parameters are given in Table 1. Our goal was to obtain the best fit to the stress curve over the widest range of stresses possible. (The operating range for the Bholin CS rheometer is  $\dot{\gamma} < 900 \text{ s}^{-1}$  and  $\tau < 400 \text{ Pa}$ .) Normally the yield stress is better determined using a direct method such as creep tests, however, while this would give a better single estimate of the yield stress, it often results in a poor fit at high stresses. Hence, we instead chose to fit all three parameters ( $\tau_Y$ ,  $K$ ,  $n$ ) using just the stress-strain-rate curve. (Note that the yield stress as measured from a creep test is still too high to explain the discrepancy between theory and experiments discussed in the main text.)

The rheological data for the Carbopol solution is typical of that seen by others [20,21]. Though there is some slight hysteresis, the data can be fit quite well to the Herschel–Bulkley constitutive model. The rheology of the Kaolin suspension, however, was more complicated. Considerable hysteresis, as well as some dependence of the measured yield stress on the sample history was observed. Also, at certain stresses the suspension would yield, but only after the stress had been applied for a fixed period of time. A dependence of the yield stress on the shear history of the suspension could explain some of our experimental observations. In the dripping experiments the fluid near the tube wall is sheared until it exits the tube. Thus, if recent shearing reduces the apparent yield stress, upon exiting the tube the Kaolin suspension may yield below the measured yield stress value. Furthermore, if the shear-history dependence is severe, it could even account for the trend of decreasing volume with  $\mathcal{W}$  observed in Fig. 11c. Such complex rheological behaviour was consistent and reproducible for our Kaolin suspension. However, we emphasize that substantially different rheology and non-Newtonian effects can be observed with different “brands” of Kaolin.

## References

- [1] J. Eggers, Nonlinear dynamics and breakup of free-surface flows, *Rev. Modern Phys.* 69 (1997) 865–929.
- [2] J. Eggers, E. Villermaux, Physics of liquid jets, *Rep. Prog. Phys.* 71 (2008) 036601.
- [3] A.M.V. Putz, T.I. Burghelca, I.A. Frigaard, D.M. Martinez, Settling of an isolated spherical particle in a yield stress shear thinning fluid, *Phys. Fluids* 20 (2008) 033102.
- [4] N. Dubash, N.J. Balmforth, A.C. Slim, S. Cochard, What is the final shape of a viscoplastic slump? *J. Non-Newt. Fluid Mech.* 158 (1–3) (2009) 91–100.
- [5] N.J. Balmforth, Y. Forterre, O. Pouliquen, The viscoplastic Stokes layer, *J. Non-Newt. Fluid Mech.* 158 (2009) 46–53.
- [6] M.R. Davidson, J.J. Cooper-White, Pendant drop formation of shear-thinning and yield stress fluids, *Appl. Math. Modelling* 30 (2006) 1392–1405.
- [7] M.A.M. Al Khatib, S.D.R. Wilson, Slow dripping of yield-stress fluids, *J. Fluids Eng.* 127 (2005) 687–690.
- [8] P. Coussot, F. Gaulard, Gravity flow instability of viscoplastic materials: the ketchup drip, *Phys. Rev. E* 72 (2005) 031409.
- [9] Q. Barral, G. Ovarlez, X. Chateau, J. Boujlel, B. Rabideau, P. Coussot, Adhesion of yield stress fluids, *Soft Matter* 6 (2010) 1343–1351.
- [10] B. Ambravaneswaran, E.D. Wilkes, O.A. Basaran, Drop formation from a capillary tube: comparison of one-dimensional and two-dimensional analyses and occurrence of satellite drops, *Phys. Fluids* 14 (2002) 2606–2620.
- [11] S.D.R. Wilson, The slow dripping of a viscous fluid, *J. Fluid Mech.* 190 (1988) 561–570.
- [12] M. Renardy, Y. Renardy, Similarity solutions for breakup of jets of power law fluids, *J. Non-Newt. Fluid Mech.* 122 (1–3) (2004) 303–312.
- [13] I.S. Gradshteyn, I.M. Ryzhik, *Table of integrals, series and products*, 4th ed., Academic Press, 1965.
- [14] O.E. Yildirim, O.A. Basaran, Deformation and breakup of stretching bridges of Newtonian and shear-thinning liquids: comparison of one- and two-dimensional models, *Chem. Eng. Sci.* 56 (1) (2001) 211–233.
- [15] R. Suryo, O.A. Basaran, Local dynamics during pinch-off of liquid threads of power law fluids: scaling analysis and self-similarity, *J. Non-Newt. Fluid Mech.* 138 (2–3) (2006) 134–160.
- [16] J. Eggers, T.F. Dupont, Drop formation in a one-dimensional approximation of the Navier–Stokes equation, *J. Fluid Mech.* 262 (1994) 205–221.
- [17] K.E. Brenan, S.L.V. Campbell, L.R. Petzold, *Numerical solution of initial-value problems in differential–algebraic equations*, SIAM, 1996.
- [18] J.G. Blom, P.A. Zegeling, A moving-grid interface for systems of one-dimensional time-dependent partial differential equations, *Tech. Rep. NM-R8904*, Centre for Mathematics and Computer Science, Stichting Mathematisch Centrum (1989).
- [19] R.M. Manglik, V.M. Wasekar, J. Zhang, Dynamic and equilibrium surface tension of aqueous surfactant and polymeric solutions, *Exp. Thermal Fluid Sci.* 25 (1–2) (2001) 55–64.
- [20] L.P. Coussot, C. Tocquer, G. Lanos, Ovarlez, Macroscopic vs. local rheology of yield stress fluids, *J. Non-Newt. Fluid Mech.* 158 (2009) 85–90.
- [21] D. Sikorski, H. Tabuteau, J.R. de Bruyn, Motion and shape of bubbles rising through a yield stress fluid, *J. Non-Newt. Fluid Mech.* 159 (2009) 10–16.